

# Garnet-doped composite polymer electrolyte with high ionic conductivity for dendrite-free lithium batteries

Linghong Xu, Guibin Li, Jianxin Guan, Lulu Wang, Jitao Chen, Junrong Zheng\*

College of Chemistry and Molecular Engineering, Peking University, Beijing, 100871, China

## ARTICLE INFO

### Keywords:

Electrochemical energy storage  
Solid polymer electrolyte  
Ceramic particles  
Lithium metal battery

## ABSTRACT

Solid polymer electrolytes are promising candidates to replace the extensively used flammable liquid electrolytes in lithium batteries. However, pure polymer electrolytes seldom meet practical requirements because of their relatively low ionic conductivity and poor mechanical properties. Herein, we report a garnet ( $\text{Li}_{6.4}\text{La}_3\text{Zr}_{1.4}\text{Ta}_{0.6}\text{O}_{12}$ , LLZTO)-doped composite polymer electrolyte (CPE) membrane for high performance lithium batteries. The CPE is composed of poly(vinylidene fluoride-co-hexafluoropropylene) (PVDF-HFP) and poly(ethylene glycol) methyl ether methacrylate (POEGMA) polymer with the addition of ceramic particles LLZTO. It not only has high ionic conductivity of  $1.00 \times 10^{-3} \text{ S cm}^{-1}$  after the activation of liquid electrolyte at room temperature, but also surprisingly restrains the growth of Li dendrites. Its electrochemical stability window is up to 4.7 V (vs.  $\text{Li}^+/\text{Li}$ ). Moreover,  $\text{LiFePO}_4/\text{Li}$  batteries using the CPE exhibit excellent cycling performance and superior rate capability.

## 1. Introduction

The exhaustion of non-renewable resources such as coal and petroleum, and the resulting environmental pollution force people to seek and develop environmentally friendly renewable energy sources such as solar energy and wind energy, which typically require energy storage devices [1,2]. Among numerous energy storage technologies, lithium batteries have the advantages of high energy density, high operating voltage, long cycle lifetime, and little memory effect. It is therefore the first choice of energy storage for many portable devices, electric vehicles and large power grids [3,4].

Lithium metal is regarded as an ideal anode for lithium batteries, because it has an unprecedented theoretical capacity ( $3860 \text{ mA h g}^{-1}$ ) and extremely low redox potential ( $\sim 3.04 \text{ V}$  vs. standard hydrogen electrodes), maximizing battery capacity density and voltage window [5,6]. However, the lithium metal is not compatible with the polyolefin separator used in traditional lithium batteries which is immersed in volatile and flammable liquid electrolytes [7]. It is prone to react with liquid organic electrolytes, resulting in the increase of battery impedance and the decrease of Coulomb efficiency [8]. In addition, commercial polyolefin separators cannot effectively inhibit the growth of lithium dendrites. Lithium dendrites can puncture through the separator and contact with the cathode, causing a short circuit [9,10]. All these factors seriously impede the application of metallic lithium in

rechargeable lithium batteries. Over the years, intensive research efforts have been devoted to solve the inherent problems of lithium metal anode, including functionalized solvents [11], various lithium salts [12,13] and electrolyte additives [14,15].

Among a variety of attempts, polymer electrolytes including gel-type and all solid state polymer electrolytes have received particular attention because of their unique properties, e.g. easy processability and leakage-proof [16]. Among the polymers that have been studied as electrolytes, such as polyacrylonitrile (PAN) [17,18], poly(vinylidene fluoride) (PVDF) [19,20], poly(ethylene oxide) (PEO) [21,22] and poly(vinyl alcohol) (PVA) [23,24], there is typically a trade-off between the mechanical properties and ionic conductivity of polymer electrolytes. All solid polymer electrolytes have good mechanical properties, but their ionic kinetic properties are limited due to low ionic conductivity and high interfacial resistance at room temperature [16,25]. On the contrary, gel polymer electrolytes have a high ionic conductivity, but poor mechanical properties [26]. Therefore, it is very necessary and urgent to develop new solid polymer electrolytes with high ionic conductivity and excellent mechanical strength.

In this study, we prepare a novel composite polymer electrolyte (CPE) that possesses both high ionic conductivity and mechanical strength. Poly(vinylidene fluoride-co-hexafluoropropylene) (PVDF-HFP) is chosen as the matrix owing to its superior electrochemical stability, thermal stability and mechanical properties [27,28], but the

\* Corresponding author.

E-mail address: [junrong@pku.edu.cn](mailto:junrong@pku.edu.cn) (J. Zheng).

<https://doi.org/10.1016/j.est.2019.100767>

Received 10 January 2019; Received in revised form 17 April 2019; Accepted 7 May 2019

Available online 20 May 2019

2352-152X/ © 2019 Elsevier Ltd. All rights reserved.

main disadvantage of PVDF-HFP is its low conductivity ( $10^{-6} - 10^{-8} \text{ S cm}^{-1}$ ) at room temperature [29]. We adopt two approaches to increase its ionic conductivity: chemically modifying the polymer and blending it with ceramic ionic conductor. In general, the introduction of chemically cross-linked structure in polymer can be an effective method to improve the dimensional stability of polymer electrolytes, and increase their ionic conductivity [30]. Inspired by this approach, we chemically attach poly(ethylene glycol) methyl ether methacrylate (POEGMA) to PVDF-HFP by polymerization reaction initiated with ultraviolet light irradiation. The O atoms on the methacryloyl group (C=O and C–O–C) have lone pair electrons that can bind  $\text{Li}^+$  ions. Adjacent methacryloyl groups are capable of transferring  $\text{Li}^+$  from one O atom to others, resulting in an enhanced ionic conductivity. Besides, garnet-type particles  $\text{Li}_{6.4}\text{La}_3\text{Zr}_{1.4}\text{Ta}_{0.6}\text{O}_{12}$  (LLZTO) with high ionic conductivity are dispersed into the polymer. The LLZTO can not only further increase the ionic conductivity of the polymer but also strengthen its mechanical properties. According to the space-charge theory, the movement of ions near the anode side is mainly driven by the electric field, leaving a space charge region, which leads to the growth of lithium metal [31]. It is conceivable that the ceramic particles and the polymer can produce a synergistic effect to restrict the movement of anions, leading to a weak space charge region near the anode side and retarding lithium dendrites formation. The composite polymer electrolyte resulted from the approach has the advantages of high ionic conductivity, wide electrochemical window, low electrode/electrolyte interfacial resistance, and good thermal stability under the activation of the organic electrolyte.

## 2. Experimental section

### 2.1. Materials

The PVDF-HFP (molecular weight of  $\sim 400,000$ ) and poly(ethylene glycol) methyl ether methacrylate (molecular weight of  $\sim 500$ ) (POEGMA) were purchased from Sigma-Aldrich. 2-Hydroxy-2-methylpropiophenone (HMPP, photo-initiator) was purchased from Macklin.  $\text{Li}_{6.4}\text{La}_3\text{Zr}_{1.4}\text{Ta}_{0.6}\text{O}_{12}$  (LLZTO), acetylene black, PVDF binder,  $\text{LiNi}_{0.5}\text{Co}_{0.2}\text{Mn}_{0.3}$  and  $\text{LiFePO}_4$  were purchased from Hefei Kejing Materials Technology Co., Ltd. Acetone was purchased from Beijing Chemical Plant. N-methylpyrrolidone (NMP) was purchased from Aladdin. The liquid electrolyte (1.0 M LiTFSI, 0.2 M  $\text{LiNO}_3$  in DOL/DME = 1/1 v/v) was purchased from Suzhou Fosai New Material Co., Ltd. The commercial lithium foil was purchased from China Energy Lithium Co., Ltd.

### 2.2. Synthesis of composite polymer electrolyte

First, 0.2 g PVDF-HFP was dissolved in acetone and the solution was stirred at  $65^\circ\text{C}$  for 3 h to form a homogeneous solution. Then, 0.2 g POEGMA and 0.04 g LLZTO were dispersed in the above PVDF-HFP solution, wherein the ratio of HMPP over POEGMA is fixed at 1%. The above mixture was stirred continuously for 10 h, and then coated on a clean glass plate, followed by UV light irradiating for 3 min. Finally, the composite electrolyte membranes ( $\sim 120 \mu\text{m}$  in thickness) were placed in vacuum oven at  $60^\circ\text{C}$  for 24 h to remove the trace of the acetone solvent. Besides CPE, pure PVDF-HFP and PPE (PVDF-HFP: POEGMA = 0.2 g: 0.2 g, without the addition of LLZTO) were also prepared. In order to enhance the interface contact between electrolyte membrane and electrodes,  $15 \mu\text{L}$  liquid electrolyte (1.0 M LiTFSI, 0.2 M  $\text{LiNO}_3$  in 1,2-dioxolane (DOL)/dimethoxymethane (DME) = 1/1 v/v) was dropped on the surface of PVDF-HFP, PPE and CPE membrane.

### 2.3. Material characterization

Scanning electron micrographs (SEM) and energy dispersive (EDS) mapping images were obtained with a field emission scanning electron

microscope (Hitachi S-4800). X-ray diffraction (XRD) data was collected with a Rigaku Ultima using  $\text{Cu K}\alpha$  radiation and  $2\theta$  in the range of  $5^\circ$  to  $80^\circ$  at  $5^\circ \text{ min}^{-1}$  to examine the crystal structure of LLZTO particles and the CPE membrane. FTIR spectroscopy was conducted using a Bruker Tensor 27 FTIR spectrometer. Thermal analyses were carried out by thermogravimetric analysis (TGA) (TA TGA-Q600) and differential scanning calorimeter (DSC) (TA Q100 DSC) in a temperature range from room temperature to  $800^\circ\text{C}$  and  $-80^\circ\text{C}$  to  $200^\circ\text{C}$  at a heating rate of  $10^\circ\text{C min}^{-1}$  under  $\text{N}_2$  atmosphere. The stress and strain curves of the membranes were recorded by a Linkam testing machine at a stretching speed of  $100 \mu\text{m s}^{-1}$  at room temperature.

### 2.4. Electrochemical measurements

The ionic conductivities of CPE were determined via the electrochemical impedance spectroscopy (EIS). The CPE membrane was sandwiched between two stainless steel (SS) blocking electrodes with a diameter of 16 mm. Data were attained using an electrochemical analyzer (CHI650C) with an amplitude voltage of 5 mV over the frequency range from 0.1 Hz to 1 MHz. The ionic conductivity ( $\sigma$ ) was calculated based on the following equation

$$\sigma = \frac{l}{R_b \cdot S} \quad (1)$$

where  $R_b$  corresponds to the bulk resistance according to EIS measurement,  $S$  is the contact area between electrode and electrolyte, and  $l$  presents the thickness of CPE membrane. Activation energy  $E_a$  of Li conduction can be calculated by the Arrhenius equation:

$$\sigma = A \exp\left(\frac{-E_a}{k_b T}\right) \quad (2)$$

where  $A$  is the pre-exponential factor,  $k_b$  is the Boltzmann constant,  $T$  is the absolute temperature, and  $E_a$  is the activation energy.

The electrochemical stability window of CPE was tested by linear sweep voltammetry (LSV) on a Li/CPE/SS cells with a working electrode of stainless steel and a counter electrode of lithium metal at a scanning rate of  $1 \text{ mV s}^{-1}$  over the potential range of 2–5 V at room temperature.

The lithium ion transfer number of CPE was measured by a combination measurements of DC polarization and AC impedance on a symmetrical cell of Li/CPE/Li and was calculated from Bruce-Vincent-Evans equation [32]

$$t_{\text{Li}^+} = \frac{I_{\text{SS}}(\Delta V - I_0 R_0)}{I_0(\Delta V - I_{\text{SS}} R_{\text{SS}})} \quad (3)$$

where  $\Delta V$  is the applied polarization voltage of 10 mV,  $I_0$  and  $R_0$  are the initial current and the initial interfacial resistance values before polarization respectively, and  $I_{\text{SS}}$  and  $R_{\text{SS}}$  are the steady-state current and the steady-state interfacial resistance value after polarization for 4 h respectively.

### 2.5. Fabrication and testing of cells

Coin-type cells (CR 2032) were assembled in an Ar-filled glove box to test the electrochemical performance of electrolyte membranes. The commercial lithium foil was used as anode. The cathode electrode slurry was mixed by  $\text{LiFePO}_4$  or  $\text{LiNi}_{0.5}\text{Co}_{0.2}\text{Mn}_{0.3}$ /acetylene black/PVDF binder with a weight ratio of 8:1:1. The N-methylpyrrolidone (NMP) was used as solvent for homogenizing all components. After stirred for 24 h, the resultant slurry was coated on aluminum current collectors by using a doctor blade. The electrodes were dried at  $100^\circ\text{C}$  for 24 h before use. The active material mass loading on the cathode foil was about  $2.8 \text{ mg cm}^{-2}$ . Coin cells were assembled in the form of cathode/CPE/Li by sandwiching the CPE between the lithium metal foil and the cathode. All the cells were tested on LANHE CT2001A battery

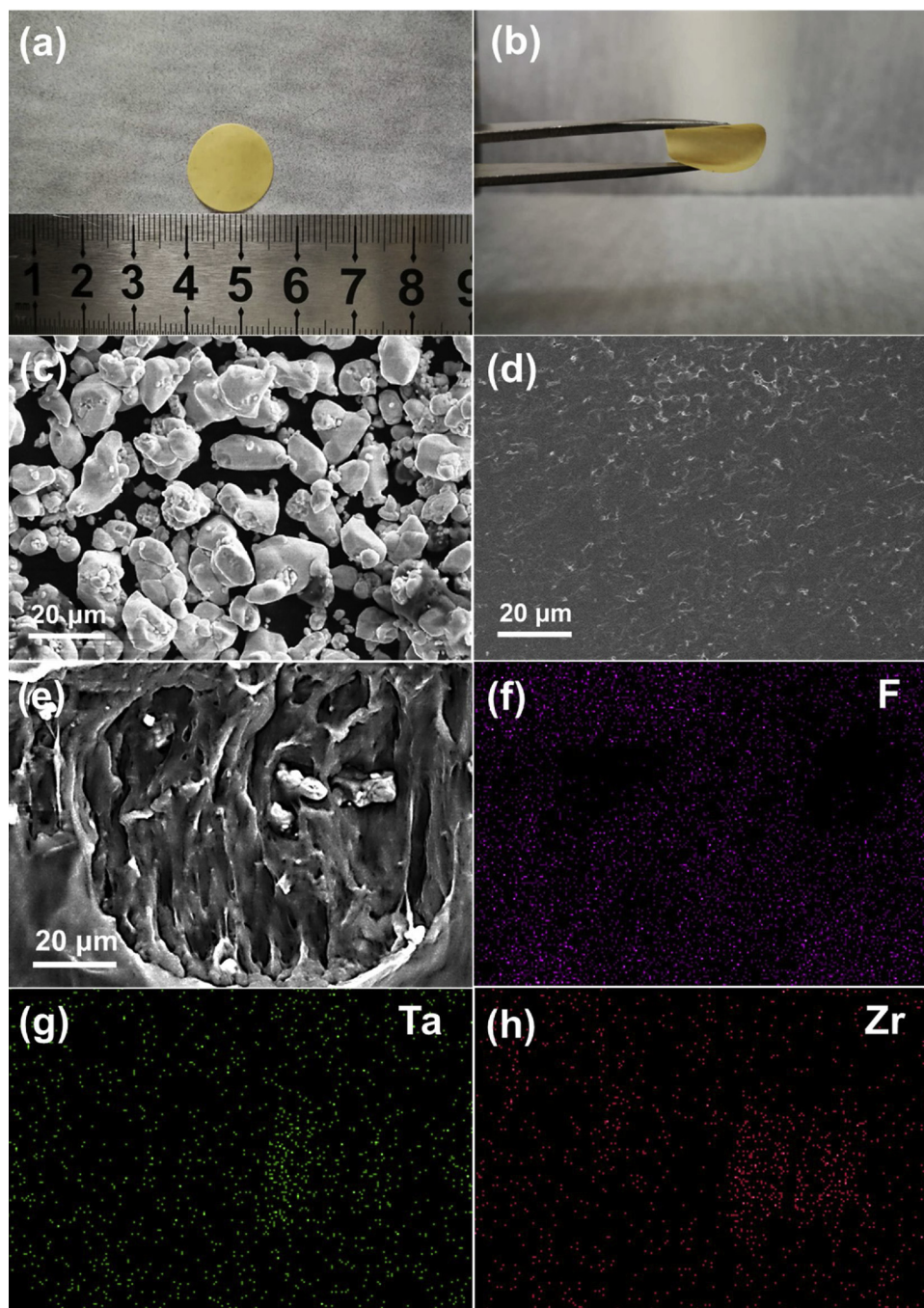


Fig. 1. Photo images of CPE membrane at (a) flat and (b) bended states. (c) SEM image of the LLZTO particles. (d) SEM image of CPE membrane. (e) The cross-section SEM image and corresponding (f–h) elemental mapping of CPE membrane.

tester (Wuhan LAND electronics Co., Ltd.) at ambient temperature.

### 3. Results and discussion

The as-obtained CPE membrane is freestanding and mechanical flexible that can be arbitrarily bent (Fig. 1a and b). The LLZTO particles of a few microns in size are well dispersed in polymer matrix (Fig. 1c and d). There are many pores with torturous structure in the cross-section SEM image (Fig. 1e), which could be attributed to phase separation between the polymer and solvent after the evaporation. The uniform distribution of pores are supposed to frustrate the direct penetration of Lithium dendrites [20]. Homogeneous distribution of F, Ta and Zr in CPE membrane are observed in Fig. 1f–h, which illustrates the

uniform incorporation of LLZTO particles in the membrane.

X-ray diffraction (XRD) is used to analyze the crystal structure. As shown in Fig. 2a, the diffraction peaks of the ceramic particles LLZTO are consistent with the standard pattern of the known garnet-type  $\text{Li}_5\text{La}_3\text{Nb}_2\text{O}_{12}$  (LLNO) (JCPDS: 80-0457). This cubic-phase garnet possesses high ionic conductivity ( $\sim 10^{-3} \text{ S cm}^{-1}$ ), a promising additive for solid state electrolyte [33–35]. The comparison in the XRD patterns indicates that the crystallinity of the polymer matrix decreases and the amorphous phase is expanded, which is contributed to the dispersion of LLZTO particles. Fourier transform infrared spectroscopy (FTIR) was used to identify the nature of functional groups present in the electrolyte membrane in the frequency range  $400\text{--}4000 \text{ cm}^{-1}$  (Fig. 2b). The characteristic peak of PVDF-HFP at  $1411 \text{ cm}^{-1}$  is attributed to the  $\alpha$ -

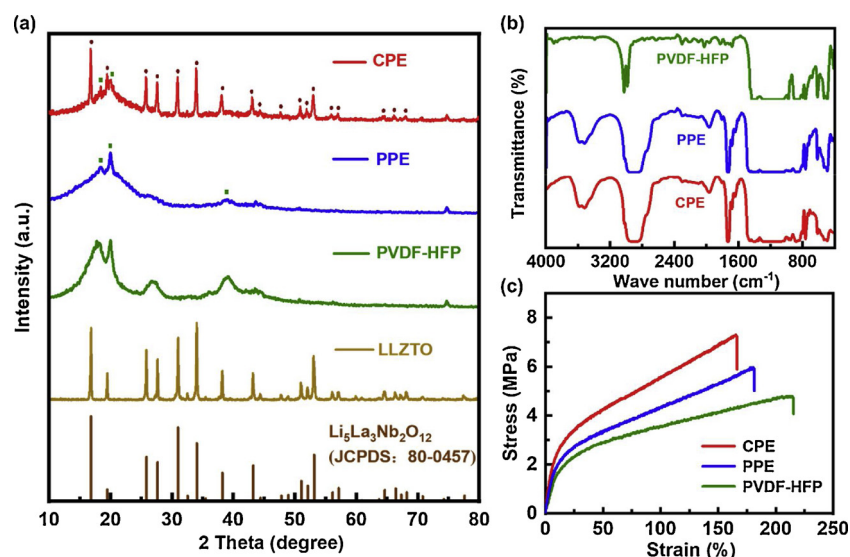


**Fig. 2.** (a) XRD patterns of CPE, PPE (PVDF-HFP: POEGMA = 0.2 g: 0.2 g, without the addition of LLZTO), PVDF-HFP, LLZTO particles and the powder diffraction file of  $\text{Li}_5\text{La}_3\text{Nb}_2\text{O}_{12}$ . (b) FTIR spectra, and (c) Stress-strain curves of the PVDF-HFP, PPE and CPE.

crystalline phase [36]. The peaks at  $532\text{ cm}^{-1}$  and  $490\text{ cm}^{-1}$  are assigned to the bending and wagging vibration of  $-\text{CF}_2$ , respectively. The peaks at  $796\text{ cm}^{-1}$  shows the stretching vibration of  $-\text{CF}_3$ . The symmetric and antisymmetric stretch vibrations of  $\text{CH}_2$  in PVDF-HFP appear at  $3025\text{ cm}^{-1}$  and  $2984\text{ cm}^{-1}$ , respectively [37,38]. The characteristic stretch vibration of  $\text{C}=\text{O}$  peak of POEGMA appears at  $1730\text{ cm}^{-1}$ . The bands at  $2862\text{--}2934\text{ cm}^{-1}$  represents the asymmetric and symmetric stretch vibrations of  $\text{CH}_2$  in POEGMA [39,40].

Outstanding mechanical properties of electrolyte membranes play a critical part in lithium batteries. The tensile strength, Young's modulus and elongation are characterized and displayed in Fig. 2c. The maximum stress of the PVDF-HFP is 4.80 MPa. After the addition of POEGMA and LLZTO, the mechanical properties of the CPE are greatly improved with a Young's modulus of 28.1 MPa and a tensile strength of 7.26 MPa. As shown in Table S1, the tensile strength of CPE is better than those of electrolyte membranes reported previously [41–43]. It is deduced that the CPE with superior mechanical properties, high toughness and tensile strength, could reduce the possibility of lithium dendrite piercing and improve the safety of lithium batteries.

To further evaluate the thermal stability of the CPE membrane, the thermogravimetric analysis (TGA) is employed. As presented in TGA curves (Fig. 3a), the initial degradation of pure PVDF-HFP occurs at  $430\text{ }^\circ\text{C}$  and is completed at  $500\text{ }^\circ\text{C}$ . With the addition of POEGMA and LLZTO, the thermal stability of the CPE membrane decreased. Before thermal degradation, a minor weight loss can be observed, which is ascribed to the trapped moisture. For the PPE and CPE membrane, the weight loss starting before  $200\text{ }^\circ\text{C}$  corresponds to the polymer melting [44]. The complete thermal decomposition of CPE membrane began at  $230\text{ }^\circ\text{C}$ , which is also stable enough for the applications in the lithium batteries. Besides TGA, the DSC curve of membrane were obtained to identify the thermal behavior of the polymer electrolyte. Fig. 3b shows that the glass transition temperature ( $T_g$ ) are reduced with the addition of POEGMA and LLZTO into PVDF-HFP from  $-31.3\text{ }^\circ\text{C}$  to  $-61.7\text{ }^\circ\text{C}$ , which indicates the crystallinity of PVDF-HFP is reduced and the amorphous region is expanded because of the plasticizing effect.

The impedance response is a characteristic feature of electrolytes, wherein the bulk resistance ( $R_b$ ) is the major contribution to the total resistance. The temperature-dependent ionic conductivity of the CPE is determined via the electrochemical impedance spectroscopy (EIS) and compared with that of the PPE and PVDF-HFP membrane (Fig. 3c). The ionic conductivity of CPE membrane reaches  $1.00 \times 10^{-3}\text{ S cm}^{-1}$  at room temperature, which is much higher than that of the pure PVDF-

HFP ( $2.92 \times 10^{-4}\text{ S cm}^{-1}$ ) and the PPE ( $5.45 \times 10^{-4}\text{ S cm}^{-1}$ ) (Fig. 3d, Fig. S1 and S2). Moreover, the ionic conductivity increases with temperature and approaches  $2.97 \times 10^{-3}\text{ S cm}^{-1}$  at  $80\text{ }^\circ\text{C}$ . As shown in Fig. 3c, the linear fitting result exhibits a typical Arrhenius-type behavior and the  $E_a$  of CPE is approximately  $0.14\text{ eV}$ , which is lower than PVDF-HFP ( $0.19\text{ eV}$ ) and PPE ( $0.18\text{ eV}$ ).  $E_a$  is considered to be the barrier for ionic conduction. The CPE with a lower activation energy denotes the low energy barrier for  $\text{Li}^+$  ion transfer. The decrease of activation energy and the enormous leap in the ionic conductivity of the CPE membrane is related to the introduction of POEGMA and LLZTO particles, which forms the  $\text{Li}^+$  transport channels and reduces the degree of crystallinity.

The  $\text{Li}^+$  ion transference number ( $t^+$ ) is a parameter that describe  $\text{Li}^+$  ion transfer ability in the electrolyte, which provides information about the rate capacity. Determination of  $t^+$  for the CPE is conducted by the combination of AC impedance and potentiostatic DC polarization (Fig. 4a). The inset of Fig. 4a shows the equivalent circuit used for the fitting to obtain bulk resistance ( $R_1$ ), interfacial resistance ( $R_2$ ) and charge transfer resistance ( $R_3$ ), constant phase element (CPE) and Warburg resistance ( $W_1$ ). The interfacial resistance of CPE increases from  $151$  to  $152.3\ \Omega$  due to the growth of SEI. The variation of current with time in the polarization process displays that the steady current reaches a value of  $2.20 \times 10^{-2}\text{ mA}$  from the initial current of  $2.50 \times 10^{-2}\text{ mA}$  before polarization. The transference number can be calculated from the Bruce-Vincent-Evans equation. Therefore, the  $t^+$  of CPE is 0.83, which is higher than that of pure PVDF-HFP (0.39) (Fig. S3) and PPE (0.65) (Fig. S4). The remarkable improvement of  $t^+$  for CPE member can be ascribed to the following factors. The oxygen atoms of  $\text{C}=\text{O}$  and  $\text{C}-\text{O}-\text{C}$  of the side chains of POEGMA contain electron pairs that are able to coordinate with  $\text{Li}^+$  ions from lithium salt, followed by an increase in salt dissociation. Meanwhile, LLZTO particles are polar. They can cooperates with PVDF-HFP to favor interactions with the lithium salt anion ( $\text{TFSI}^-$ ), thus preventing the movement of the anion ( $\text{TFSI}^-$ ) and enhancing the lithium ion transference number. The high cationic movement can be beneficial to alleviate polarization, boosting the rate capacity and suppress the formation of lithium dendrites.

Asymmetrical cells of Li/electrolyte-membrane/stainless steel are assembled to estimate the electrochemical stability window of the electrolytes membrane. Fig. 4b shows the comparison of liner sweep voltammetry (LSV) curves of the pure PVDF-HFP, PPE and CPE membrane at a scan rate of  $1\text{ mV s}^{-1}$ . In the pure PVDF-HFP membrane, the

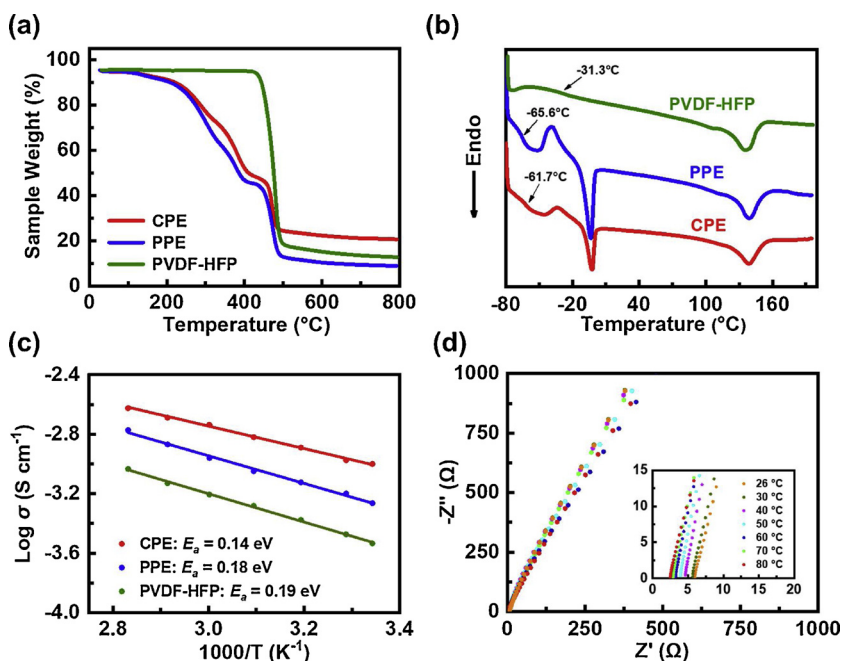


Fig. 3. (a) TGA and (b) DSC curves of the membranes. (c) Arrhenius plots of the CPE at temperatures from 20 to 80 °C. (d) The impedance spectra of the CPE in stainless steel (SS) | Electrolyte | SS sandwich cell at temperatures from 20 to 80 °C.

current starts to increase obviously at  $\sim 4.5$  V (vs.  $\text{Li}^+/\text{Li}$ ). This corresponds to the oxidative decomposition potential of the electrolyte. When the POEGMA and LLZTO are introduced into the electrolyte membrane, the electrochemical stability of CPE is slightly increased to  $\sim 4.7$  V (vs.  $\text{Li}^+/\text{Li}$ ). The cells with  $\text{LiNi}_{0.5}\text{Co}_{0.2}\text{Mn}_{0.3}$  cathode are tested at a rate of 0.2C ( $1\text{C} = 200\text{ mA h g}^{-1}$ ). As shown in Fig. 4c, the cell with liquid electrolyte displays lower capacity while the charging voltage reaches 4.5 V. In contrast, the cell using CPE shows the smooth curves and less capacity loss, which indicates that the electrochemical stability of CPE during charging and discharging (Fig. 4d).

The dynamical stability test of the Li/electrolyte interface is performed to assess the electrochemical stability of electrolyte membrane against the lithium metal. In this experiment, a constant current density of  $0.1\text{ mA cm}^{-2}$  with a half testing cycle of 1 h is carried out in symmetric Li/electrolyte membrane/Li cells. The Li continuously stripes/plates in electrodes and the corresponding curve of voltage changing

over time is obtained. The voltage as well as the cell resistance is expected to drop suddenly with the formation of Li dendrites, indicating the short circuit of the cell. As shown in Fig. 5a, the cell using CPE membrane shows excellent cycle stability in 800 h cycling measurements. The detailed voltage curve of the CPE cell at 100–108 h, 400–408 h, 700–708 h (the insets of Fig. 5a) presents the flat voltage plateau during the entire cycling process at a low overpotential of about 13 mV without short circuiting. Evidently, the CPE membrane shows highly stable lithium stripping/plating cycling reversibility, and the Li dendrites growth has been considerably restrained. As a sharp contrast, the interface is unstable in the pure PVDF-HFP membrane with a higher voltage plateau of 17 mV. A sudden voltage drop is detected after 350 h cycling, possibly caused by the internal short circuit induced by the Li dendrite formation. Besides, the symmetric cell using the designed CPE is tested with higher current density of  $1\text{ mA/cm}^2$ . As shown in Fig. S5, the cell with CPE exhibits a stable voltage profile over long-term cycling

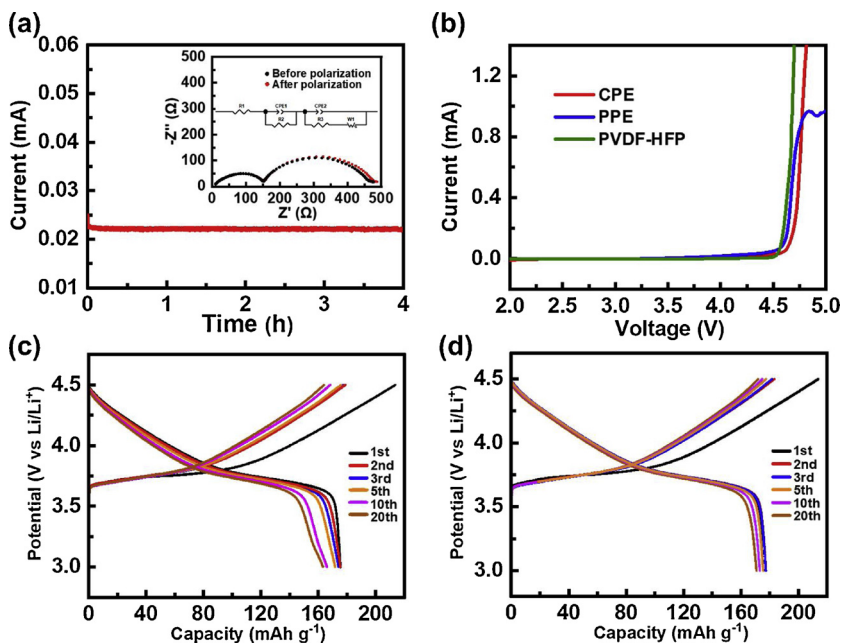


Fig. 4. (a) Current-time profile of a symmetrical Li/CPE/Li cell after applying a DC voltage of 10 mV on the cell. The inset shows the Nyquist impedance spectra and equivalent circuit of the cell before and after polarization. (b) Comparison of linear sweep voltammograms of PVDF-HFP, PPE and CPE. Charge-discharge curves of (c)  $\text{LiNi}_{0.5}\text{Co}_{0.2}\text{Mn}_{0.3}$ /liquid electrolyte/Li and (d)  $\text{LiNi}_{0.5}\text{Co}_{0.2}\text{Mn}_{0.3}$ /CPE/Li at a rate of 0.2C.

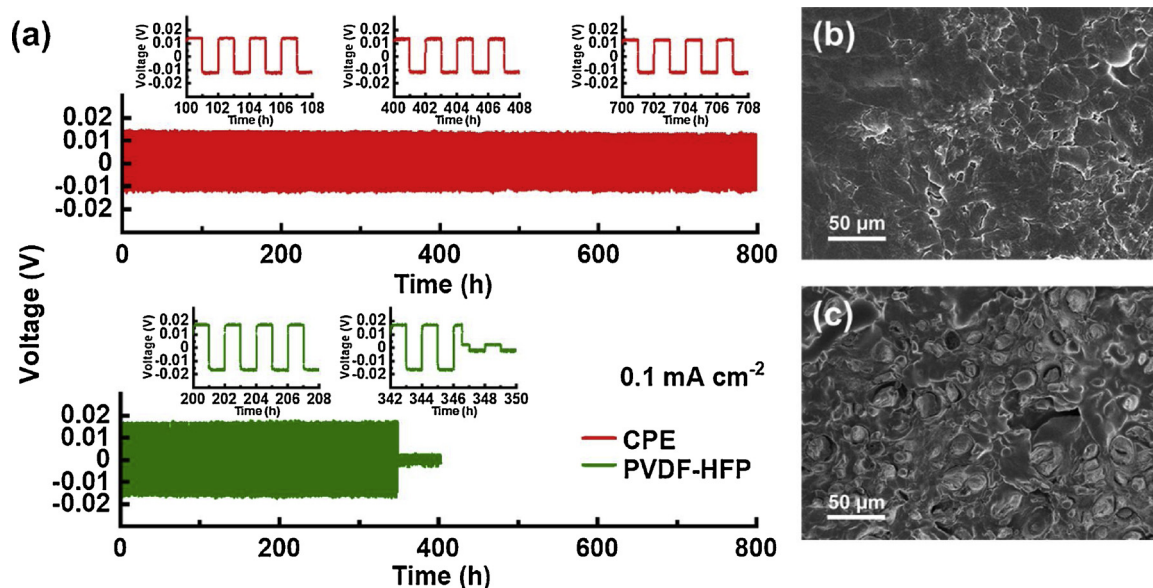


Fig. 5. (a) Voltage profiles of lithium stripping/plating experiments of symmetric lithium cells for CPE and PVDF-HFP at a current density of  $0.1 \text{ mA cm}^{-2}$ . (b) SEM image of a lithium anode polarized in CPE after 800 h cycling at  $0.1 \text{ mA cm}^{-2}$ . (c) SEM image of a lithium anode polarized in PVDF-HFP after 400 h cycling at  $0.1 \text{ mA cm}^{-2}$ .

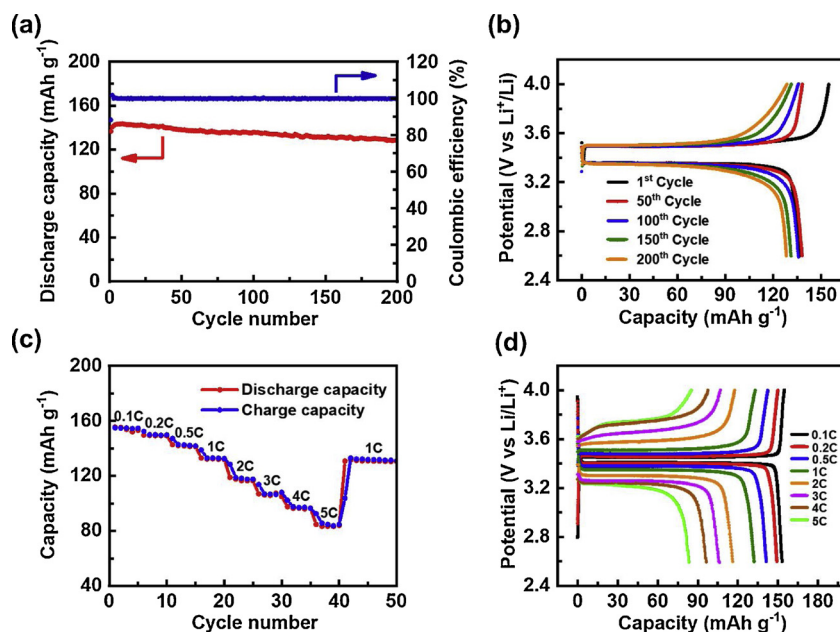


Fig. 6. Electrochemical cycling performance of the CPE membrane in the  $\text{LiFePO}_4/\text{CPE}/\text{Li}$  battery at room temperature. (a) Cycling performance and (b) typical charge-discharge curves at a rate of 0.5C. (c) Rate capacity and (d) corresponding galvanostatic discharge/charge voltage curves.

with an overpotential of about 150 mV. Contrastingly, the overpotential of the cell using PVDF-HFP increases from 140 mV to 340 mV under the same conditions. It can be inferred that the CPE displays a better cycling stability under large current density.

To further observe the morphologies of the Li metal electrode surface after galvanostatic cycling measurements, the cycled symmetric cells are disassembled in the state of stripping for SEM analysis. As shown in Fig. 5b, the Li metal electrode of CPE cell maintain a relatively flat surface without any noticeable lithium dendrites. However, the Li metal electrode in the pure PVDF-HFP cell is covered by the granular dendrites (Fig. 5c). The images suggest that the CPE membrane can effectively suppress the growth of lithium dendrites, which may be attributed to the LLZTO. The addition of the LLZTO particles not only increases the ionic conductivity, but also enhances the rigidity of the

CPE membrane.

With outstanding electrochemical and mechanical properties tested, the CPE membrane is applied in lithium batteries. Cells of  $\text{LiFePO}_4$  as the cathode and Li metal as the anode are assembled to demonstrate the cycling performance as well as the rate capability. The cycling performance and the galvanostatic charge-discharge curves of  $\text{LiFePO}_4/\text{CPE}/\text{Li}$  batteries are shown in Fig. 6a and b, respectively. The cells with CPE membrane display better reversible capacity at a rate of 0.5C ( $1\text{C} = 170 \text{ mA h g}^{-1}$ ) and a high capacity retention of 94.6% after 200 cycles (first at  $136.6 \text{ mA h g}^{-1}$  and 200th, at  $129.2 \text{ mA h g}^{-1}$ ) with a slight increase in overpotential. Another cycling test with a higher rate of 1C is completed, and the capacity remained at 90.3% of its initial capacity after 200 cycles (Fig. S6). The above results indicate that the CPE possesses good interfacial compatibility with electrodes during

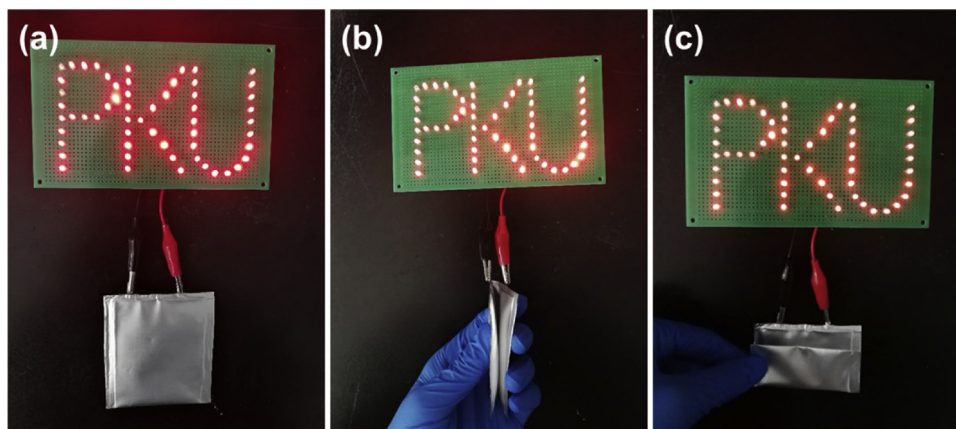


Fig. 7. The LED lamps pattern can be lighted under (a) flatted and (b and c) bent.

charging and discharging. By comparison, the discharge capacity of the cells containing pure PVDF-HFP membrane rapidly decreases with cycle. A lower reversible capacity and capacity retention (85.6% at 0.5C rate and 81.7% at 1C rate) are detected over 200 cycles (Fig. S7 and S8). The surface SEM images of the Li metal electrode after 200 cycles (Fig. S9) indicate that the CPE membrane effectively inhibits the growth of lithium dendrites. In contrast, the Li metal in the PVDF-HFP cell is covered by massive dendrites, which continuously destroys the SEI film during cycling resulting in a degradation of the capacity. The remarkable cycle performance of the CPE membrane can be ascribed to better electrochemical interface stability as observed in the impedance tests. Besides, the high Columbic efficient (~100%) throughout the cycling test is shown in the Fig.6a, reflecting the excellent charge-transfer reversibility through the electrode/electrolyte interface.

Fig. 6c shows the rate performance of LiFePO<sub>4</sub>/Li batteries with CPE membrane. The capacities decrease with an increase of the current density, which is caused by aggravated polarization. Compared with the cell using pure PVDF-HFP that has lower discharge capacity at high rates (Fig. S10), the cell with CPE can attain higher discharge capacity (~83 mA h g<sup>-1</sup>) at 5C. Moreover, the capacity recovers to 131 mA h g<sup>-1</sup> when the current density is switched from 5C back to 1C after 40 cycles. These results clearly indicate that the CPE membrane exhibits lower polarization, which is the positive effects of high lithium transfer number. The outstanding LiFePO<sub>4</sub>/CPE/Li cell performance confirms that with the newly developed CPE membrane, the Li metal anode is feasible for use in practical batteries

In addition to the coin-type cells, a soft packed LiFePO<sub>4</sub>/Li battery was assembled with LiFePO<sub>4</sub> as the cathode, lithium strip as the anode, and CPE as the electrolyte. As shown in Fig. 7, because of excellent interfacial compatibility between electrodes and CPE, the LiFePO<sub>4</sub>/Li soft packed battery can steadily light up the LED lamps pattern no matter under flatted and bent. These results indicate the potential application of the CPE membrane in flexible devices.

#### 4. Conclusion

In conclusion, a flexible composite polymer electrolyte membrane has been successfully prepared. The soft part of polymer possesses numerous methacryloyl groups to coordinate with Li<sup>+</sup> ions, resulting in high ionic conductivity, and its rigid part - LLZTO particles improve the mechanical strength of the electrolyte membrane to effectively restrain lithium dendrites growth. The CPE shows a wide electrochemical stability window up to 4.7 V (vs. Li<sup>+</sup>/Li) and high ionic conductivity of 1.00 × 10<sup>-3</sup> S cm<sup>-1</sup> at room temperature. LiFePO<sub>4</sub>/Li batteries with the CPE membrane display an initial discharge of 136.6 mA h g<sup>-1</sup> at 0.5C rate, with 94.6% capacity retention after 200 cycles. Besides, the CPE exhibits high Columbic efficient (~100%) and excellent rate capability compared with pure PVDF-HFP. All these results demonstrate that the

CPE have great potential for high energy density lithium batteries.

#### Acknowledgements

This material is based upon work supported by Fujian Minhua Power Source Co., Ltd, National Science Foundation of China (NSFC-21627805, 21673004, and 21821004) and MOST (2017YFA0204702) China.

#### Appendix A. Supplementary data

Supplementary material related to this article can be found, in the online version, at doi:<https://doi.org/10.1016/j.est.2019.100767>.

#### References

- [1] J.M. Tarascon, M. Armand, *Nature* 414 (2001) 359–367.
- [2] M. Armand, J.M. Tarascon, *Nature* 451 (2008) 652–657.
- [3] V. Etacheri, R. Marom, E. Ran, G. Salitra, D. Aurbach, *Energy Environ. Sci.* 4 (2011) 3243–3262.
- [4] P.V. Braun, J. Cho, J.H. Pikul, W.P. King, H. Zhang, *Curr. Opin. Solid State Mater. Sci.* 16 (2012) 186–198.
- [5] X.B. Cheng, R. Zhang, C.Z. Zhao, Q. Zhang, *Chem. Rev.* 117 (2017) 10403–10473.
- [6] D. Li, L. Chen, T. Wang, L.Z. Fan, *ACS Appl. Mater. Interfaces* 10 (2018) 7069–7078.
- [7] S.E. Sloop, J.K. Pugh, S. Wang, J.B. Kerr, K. Kinoshita, *Electrochim. Solid-State Lett.* 4 (2001) 357–364.
- [8] H. Zhou, Y. Wang, H. Li, P. He, *Chemsuschem.* 3 (2010) 1009–1019.
- [9] M.S. Whittingham, *Chem. Rev.* 35 (2004) 4271–4301.
- [10] J. Chen, *Materials* 6 (2013) 156–183.
- [11] B. Pohl, M. Grünebaum, M. Drews, S. Passerini, M. Winter, H.D. Wiemhöfer, *Electrochim. Acta* 180 (2015) 795–800.
- [12] S.S. Zhang, *Electrochem. commun.* 8 (2006) 1423–1428.
- [13] H. Chen, M. Armand, M. Courty, M. Jiang, C.P. Grey, F. Dolhem, J.M. Tarascon, P. Poizat, *J. Am. Chem. Soc.* 131 (2009) 8984–8988.
- [14] X.Q. Zhang, X.B. Cheng, X. Chen, C. Yan, Q. Zhang, *Adv. Funct. Mater.* 27 (2017) 1605989.
- [15] S.Z. Sheng, *J. Power Sources* 162 (2006) 1379–1394.
- [16] C. Sun, J. Liu, Y. Gong, D.P. Wilkinson, J. Zhang, *Nano Energy* 33 (2017) 363–386.
- [17] Y.W. Chen-Yang, H.C. Chen, F.J. Lin, C.C. Chen, *Solid State Ion.* 150 (2002) 327–335.
- [18] H.R. Jung, D.H. Ju, W.J. Lee, X. Zhang, R. Kotek, *Electrochim. Acta* 54 (2009) 3630–3637.
- [19] A. Magistris, P. Mustarelli, E. Quartarone, P. Piaggio, A. Bottino, *Electrochim. Acta* 46 (2001) 1635–1639.
- [20] Aravindan Vickraman, Jayachandran Srinivasan, *Eur. Phys. J-Appl. Phys.* 45 (2009) 11101.
- [21] L. Chen, Y. Li, S.-P. Li, L.-Z. Fan, C.-W. Nan, J.B. Goodenough, *Nano Energy* 46 (2018) 176–184.
- [22] S. Kim, E.J. Hwang, S.J. Park, *Curr. Appl. Phys.* 8 (2008) 729–731.
- [23] V.M. Mohan, W. Qiu, J. Shen, W. Chen, *J. Polym. Res.* 17 (2010) 143–150.
- [24] P.B. Bhargav, V.M. Mohan, A.K. Sharma, V.V.R.N. Rao, *Int. J. Polym. Mater.* 56 (2007) 579–591.
- [25] D. Zhou, Y.-B. He, Q. Cai, X. Qin, B. Li, H. Du, Q.-H. Yang, F. Kang, *J. Mater. Chem. A Mater. Energy Sustain.* 2 (2014) 20059–20066.
- [26] D.T.H. Jr, N.P. Balsara, *Annu. Rev. Mater. Res.* 43 (2013) 503–525.
- [27] M. Stolarzka, L. Niedzicki, R. Borkowska, A. Zalewska, W. Wieczorek, *Electrochim. Acta* 53 (2008) 1512–1517.

- [28] H. Luo, C. Chen, K. Zhou, X. Zhou, Z. Wu, D. Zhang, RSC Adv. 5 (2015) 68515–68522.
- [29] S. Ramakumar, C. Deviannapoorani, L. Dhivya, L.S. Shankar, R. Murugan, Prog. Mater. Sci. 88 (2017) 325–411.
- [30] Q. Zheng, L. Ma, R. Khurana, L.A. Archer, G.W. Coates, Chem. Sci. 7 (2016) 6832–6838.
- [31] C.Z. Zhao, X.Q. Zhang, X.B. Cheng, R. Zhang, R. Xu, P.Y. Chen, H.J. Peng, J.Q. Huang, Q. Zhang, P. Natl, Acad. Sci. USA. 114 (2017) 11069–11074.
- [32] J. Evans, C.A. Vincent, P.G. Bruce, Polymer 28 (1987) 2324–2328.
- [33] W. Luo, Y. Gong, Y. Zhu, K.K. Fu, J. Dai, S.D. Lacey, C. Wang, B. Liu, X. Han, Y. Mo, J. Am. Chem. Soc. 138 (2016) 12258–12262.
- [34] X. Han, Y. Gong, K. Fu, X. He, G.T. Hitz, J. Dai, A. Pearse, B. Liu, H. Wang, G. Rubloff, Nat. Mater. 16 (2017) 572–579.
- [35] C. Yang, B. Liu, F. Jiang, Y. Zhang, H. Xie, E. Hitz, L. Hu, Nano Res. 10 (2017) 4256–4265.
- [36] Y. Feng, W.L. Li, Y.F. Hou, Y. Yu, W.P. Cao, T.D. Zhang, W.D. Fei, J. Mater. Chem. C Mater. Opt. Electron. Devices 3 (2015) 1250–1260.
- [37] Shalu, V.K. Singh, R.K. Singh, J. Mater. Chem. C Mater. Opt. Electron. Devices 3 (2015) 7305–7318.
- [38] D. Saikia, A. Kumar, Eur. Polym. J. 41 (2005) 563–568.
- [39] Z. Du, X. Sun, X. Tai, G. Wang, X. Liu, RSC Adv. 5 (2015) 17194–17201.
- [40] N. Grishkewich, S.P. Akhlaghi, Y. Zhaoling, R. Berry, K.C. Tam, Carbohydr. Polym. 144 (2016) 215–222.
- [41] Q. Wang, W.-L. Song, L.-Z. Fan, Y. Song, J. Membrane Sci. 492 (2015) 490–496.
- [42] J. Zhang, X. Zang, H. Wen, T. Dong, J. Chai, Y. Li, B. Chen, J. Zhao, S. Dong, J. Ma, L. Yue, Z. Liu, X. Guo, G. Cui, L. Chen, J. Mater. Chem. A Mater. Energy Sustain. 5 (2017) 4940–4948.
- [43] S. Klongkan, J. Pumchusak, Electrochim. Acta 161 (2015) 171–176.
- [44] W.H. Hou, C.Y. Chen, C.C. Wang, Y.H. Huang, Electrochim. Acta 48 (2003) 679–690.